Non-Born-Oppenheimer electronic wave packet in molecular nitrogen at 14 eV probed by time-resolved photoelectron spectroscopy

Marceau, Claude; Makhija, Varun; Peng, Peng; Hervé, Marius; Corkum, P. B.; Naumov, A. Yu.; Stolow, A.; Villeneuve, D. M.

Publisher's version / Version de l'éditeur:
https://doi.org/10.1103/PhysRevA.99.023426
Physical Review A, 99, 2, 2019-02-26

Non-Born-Oppenheimer electronic wave packet in molecular nitrogen at 14 eV probed by time-resolved photoelectron spectroscopy

Claude Marceau,[1,*] Varun Makhija,[2] Peng Peng,[1] Marius Hervé,[1] P. B. Corkum,[1] A. Yu. Naumov,[1] A. Stolow,[2,3,4] and D. M. Villeneuve[1]

[1]*Joint Attosecond Science Laboratory, National Research Council and University of Ottawa, 100 Sussex Drive, Ottawa, Ontario, Canada K1A 0R6*

[2]*Department of Physics, University of Ottawa, 598 King Edward, Ottawa, Ontario, Canada K1N 6N5*

[3]*Department of Chemistry, University of Ottawa, 10 Marie Curie, Ottawa, Ontario, Canada K1N 6N5*

[4]*National Research Council, 100 Sussex Drive, Ottawa, Ontario, Canada K1A 0R6*

(Received 30 August 2018; published 26 February 2019)

We report the observation of a 4.1 ± 0.2 THz quantum beat in the photoelectron spectrum of molecular nitrogen following coherent optical excitation by 14 eV photons and probed by two photons at 800 nm. The intermediate states in the two pathway interference are the valence state $b'\ ^1\Sigma_u^+\ v = 13$ and Rydberg state $c_4'\ ^1\Sigma_u^+\ v = 4$. The amplitude of the coherent oscillations decays in about 3 ps and does not revive. Opposite phases in the photoelectron yield corresponding to different vibrational levels of the final cationic states $X^2\Sigma_g^+\ v = 0$, $A\ ^2\Pi_u\ v = 1$, and $X^2\ \Sigma_g^+\ v = 2, 3, 4$ are reported. Simulation results show that the interference originates from the strongly mixed character of the two simultaneously excited eigenstates, causing large population oscillations in the zeroth-order Born-Oppenheimer diabatic basis. No quantum beat was observed when probing with single photon at 400 nm, suggesting a resonance with a state just below the ionization potential which acts as a filter, improving the quantum beat contrast.

DOI: 10.1103/PhysRevA.99.023426

I. INTRODUCTION

The availability of ultrafast laser systems delivering femtosecond pulses in the millijoule regime has allowed the fields of femtochemistry [1] and attosecond science [2] to flourish. In a typical femtosecond time-domain spectroscopy experiment, a resonant optical pulse prepares a state or a coherent superposition of states (by definition, a wave packet) of interest in the molecular target. This wave packet could be neutrally dissociative [3], singly ionized [4], or a coherent superposition of bound vibrational [5], electronic [6], or spin-orbit states [7]. Wave packets may be detected, for example, by recording the kinematic properties of the ejected particles (electrons, ions) after a second (probe) laser pulse has projected the wave packet onto a final state which acts as a template [8,9].

Time-resolved photoelectron spectroscopy (TRPES) is particularly effective at disentangling excited state nonadiabatic dynamics, driven by the derivative couplings between electronic states, the failure of the Born-Oppenheimer (BO) approximation [8,10–12], an important aspect of chemical dynamics in polyatomic molecules. We previously described the two limiting cases for Koopman's ionization correlations in TRPES. The first case, complementary ionization correlations, is when the excited electronic states in the wave packet each project onto different photoelectron continua [13]. The second case, corresponding ionization correlations, is when the excited electronic states in the wave packet each project onto the same photoelectron continuum [14]. In this latter case, of which N_2 is an example, the wave-packet evolution may still be monitored via the vibrationally resolved photoelectron spectrum, as we show here. However, in polyatomic systems, such dynamics tend to appear irreversible due to the high density and irregular level spacings involved: net population is transferred from one electronic state to another. Due to the highly complex couplings in polyatomics, their dynamical description is often phenomenological. Here we applied TRPES to the simple homonuclear diatomic N_2 where a pair of electronic states was coherently prepared by a 14 eV ultrashort pulse. Oscillation of zeroth-order population between these electronic states, driven by nonadiabatic coupling, was observed in the vibrationally resolved photoelectron spectrum via two-photon ionization with an 800 nm probe pulse. This permits a quantitative description of the nonadiabatic dynamics, as described herein.

Prior resonantly enhanced multiphoton ionization (REMPI) studies of nitrogen probed various excited states in the 8.6–13.6 eV range, namely, $o_3\ ^1\Pi_u\ v = 1$–2 [15], $b\ ^1\Pi_u\ v = 0$–5, $c\ ^1\Pi_u\ v = 0$–1, $c'\ ^1\Sigma_u^+\ v = 0$–1, $a\ ^1\Pi_g\ v = 0$–5 [16], and $a\ ^1\Pi_g\ v = 10$–14 [17]. Electron impact was also used to study the extreme ultraviolet emission spectrum of nitrogen, and signs of strong homogeneous configuration interactions were observed between the $b'^1\Sigma_u^+$ state and the Rydberg state $c_4'^1\Sigma_u^+$ [18]. The homogeneous valence-Rydberg interaction between these two $^1\Sigma_u^+$ electronic states, resulting from the crossing of two diabatic potential energy curves of the same symmetry, has been extensively studied theoretically [19–21].

*claude.marceau@nrc-cnrc.gc.ca

In this work, we report the observation of a 4.1 ± 0.2 THz oscillation in the two-photon ionization photoelectron yield from molecular nitrogen following a coherent 14 eV ($\sim$89 nm) vacuum ultraviolet excitation. These oscillations are attributed to the coherent exchange of population between the highly vibrationally excited valence state $b'^1\Sigma_u^+$ $v = 13$ and the Rydberg state $c_4'^1\Sigma_u^+$ $v = 4$. We present a simple model based on vibrational wave function overlap integrals which captures the essence of the wave packet and qualitatively reproduces the experimental results.

II. EXPERIMENT

The experimental setup and data analysis were previously reported [22]. Laser pulses from a commercial Ti:Sapphire laser system at 100 Hz were split by a beam splitter. About 3 mJ were frequency doubled by a 500 μm β-BBO crystal, then passed through a birefringent delay-compensating calcite plate. The 800 nm component was then rotated in polarization by a half-wave plate, and sum frequency to 267 nm was finally achieved by a 150 μm thick β-BBO. The 800 nm and 400 nm components were then separated by dichroic mirrors. The 267 nm pulses (about 200 μJ, 70 fs) were sent into a vacuum chamber where they were focused inside an argon pulsed gas jet, generating detectable high harmonics of the 267 nm driver with order 3, 5, and 7. These 267 nm harmonics were centered, respectivel,y around 14.0 eV (H3), 23.3 eV (H5), and 32.6 eV (H7) in photon energy. The high harmonic beam was recombined collinearly with the 800 nm beam by a mirror with a hole. Both beams were then focused by a gold-coated toroidal mirror inside a velocity map imaging spectrometer (VMI) where they interacted with a pulsed beam of molecular nitrogen (Fig. 1). The delay was varied between the two pulses by steps of 26 fs. The focused intensity of the 800 nm probe pulse was about 2×10^{13} W/cm^2 with a pulse duration about 80 fs with a slight positive chirp. Note that similar results were obtained with 50 fs 800 nm pulses of various peak intensities.

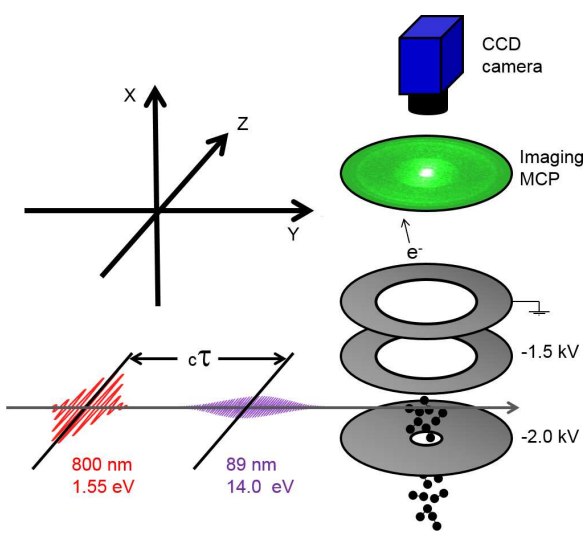

FIG. 1. Schematic representation of the experimental setup. The velocity map imaging spectrometer collects 2D photoelectron momentum angular distributions as a function of pump-probe delay. The third momentum component ($\mathbf{p_X}$) can be recovered by Abel inversion as cylindrical symmetry is preserved along the polarization direction (Z).

Photoelectron angular distributions were recorded by the VMI spectrometer as a function of the pump-probe delay. The background probe only above the threshold ionization spectrum was subtracted from the experimental data. Since all polarizations were linear and parallel, cylindrical symmetry was preserved and the images could be Abel inverted to get the full 2D cross sections using the pBaseX algorithm [23].

Various experimental techniques were used to gain insight into the physics, and we just list them here. Two different probe wavelengths were used, 800 nm and 400 nm. The peak intensity of the probe pulse was tuned using a variable neutral density filter. Different thin metal foils were inserted in the pump beam to confirm which harmonic of 267 nm was responsible for initiating the quantum beat. The fundamental central pump photon energy was experimentally tuned by varying the phase-matching angle of the two β-BBO crystals. The polarization of the probe was controlled by a half-wave plate to allow for perpendicular pump-probe polarization measurements.

III. RESULTS

The time-resolved photoelectron yield integrated over all angles is shown in Fig. 2(a) for the 800 nm multiphoton probe case. A clear blurring of the photoelectron spectrum by the AC Stark shift, accompanied by the appearance of sum frequency processes with one or more probe photons, is seen at delay zero. Low-energy photoelectron structures are seen above delay zero. Interesting yield oscillations of frequency 4 THz are very obvious in Fig. 2(a). Three photoelectron spectra averaged, respectively, before delay zero, after delay zero around one phase, and around the opposite phase of the 4 THz oscillations are shown in Fig. 2(b). Features between 0.55 and 0.80 atomic units of momentum in Figs. 2(a) and 2(b) come from single-photon ionization by the fifth harmonic of 267 nm. This is obviously insensitive in TRPES to the pump-probe delay (since the electron was already emitted) except at delay zero, where the Stark effect can play a role. Molecular axis alignment and rotational revivals do affect the laboratory frame photoelectron angular distributions from the single-photon process when the infrared pulse arrives first (negative delays). This was the topic of our recent work [22].

We performed additional measurements with identical pump step but probing done with a relatively weak 400 nm pulse ($I < 10^{12}$ W/cm^2, 50 fs). The corresponding time-resolved photoelectron spectrum and final cationic state assignments are shown in Figs. 3(a) and 3(b), respectively. There are similarities between the strong field 800 nm probing [Fig. 2(a)] and the weak field 400 nm probing [Fig. 3(a)], namely, the onset of low-energy photoelectrons for positive delays. The main observed difference is the absence of a quantum beat when using a 400 nm probe.

Photoelectron angular distributions were integrated over selected final state cationic channels for the 800 nm probe case. The yields as a function of delay are presented in Fig. 4. Strong oscillations are clearly seen in most channels for delays greater than 0.6 ps but are damped as the delay increases. Similar oscillations are also seen in some channels for the

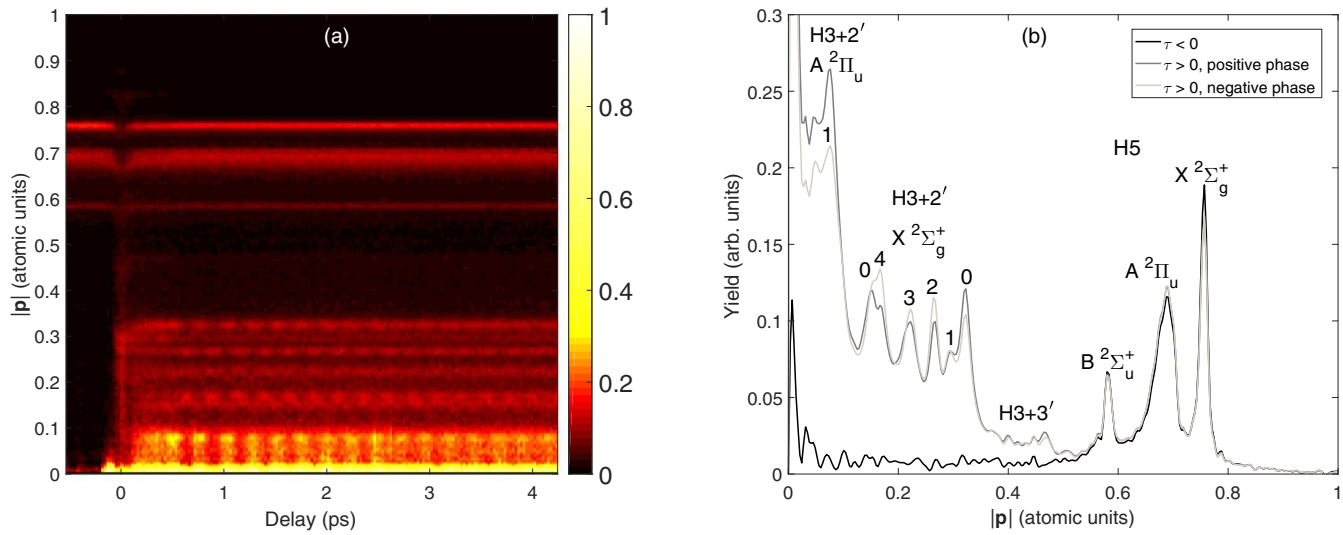

FIG. 2. (a) Map of the angle-averaged photoelectron spectrum of N_2 following 14 eV pump excitation and 800 nm multiphoton probe, as function of pump-probe time delay. Positive delay means that the 800 nm probe follows the 14 eV pump. (b) Integrated photoelectron yield versus photoelectron momentum averaged over three time-delay windows. The ionization processes and final cationic states are labeled. The $H3 + 2'$ process is of most interest because it is vibrationally resolved. Photoelectrons with momentum above 0.55 atomic unit of momentum (>4 eV) come from single-photon ionization by the fifth harmonic of 267 nm and are assigned to three different electronic final states of N_2^+.

asymmetry parameters, and therefore these are not shown here. Fourier transforms in the range 0.6 to 4 ps with 128 points are presented in Fig. 5 for the different channels of the yield. To estimate the decay rate of the oscillations, a short-time Fourier transform analysis was performed on the various channels of the yields (Fig. 6). Exponential decays were fitted to the 4.1 THz component of the yield for the various channels, and the resulting time constants ranged between 2.5–4.0 ps.

The following experimental tests were performed to confirm which harmonic of 267 nm initiated the observed quantum beat. First, a series of measurements was taken with a 200 nm thick aluminum foil in the pump beam. This filter completely blocked the 267 nm light and its third harmonic but transmitted about 5% and 10% of the fifth and seventh harmonic, respectively. The 4.1 THz quantum beats in the photoelectron spectrum disappeared. A second test was to introduce a 100 nm thick indium filter in the pump beam. This had the effect of completely blocking the fundamental 267 nm radiation while transmitting about 15% of the third harmonic and less than 1% of the fifth and seventh harmonics. The quantum beats at 4.1 THz were still observable. A third test was done with the high-harmonic pulsed gas jet turned off. There was therefore only 267 nm present but none of its harmonics. No low-energy photoelectrons were observed. These three tests confirm that the observed quantum beat is

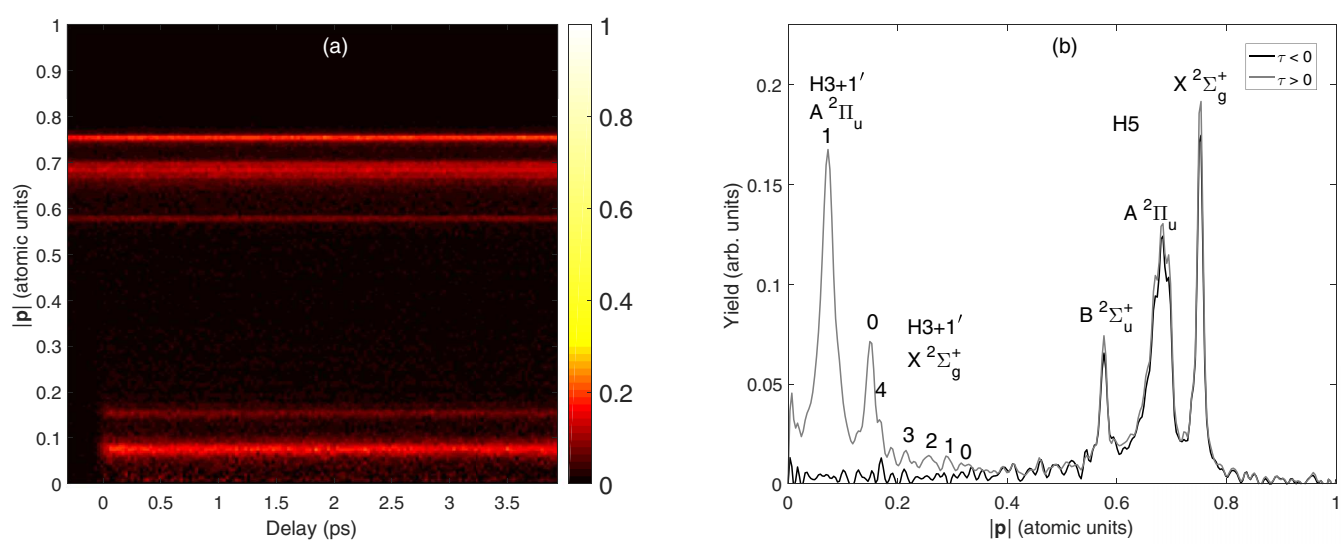

FIG. 3. (a) Time-domain photoelectron spectrum of N_2 following 14 eV pump excitation and weak field 400 nm single-photon probing. (b) Integrated photoelectron yield versus photoelectron momentum averaged over two time-delay windows.

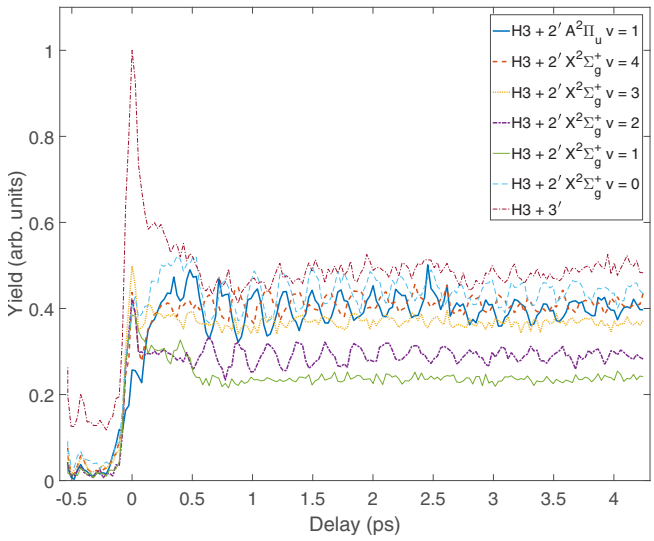

FIG. 4. Photoelectron yield for selected ionization channels as function of pump-probe time delay. The 4.1 THz quantum beat is clearly seen.

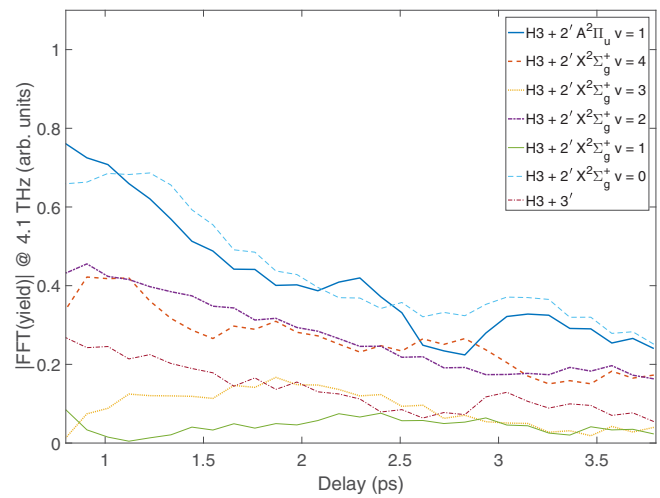

FIG. 6. Short-time Fourier transform amplitude of the photoelectron yield taken at 4.1 THz with a bin width of 0.58 THz. No evidence of rotational structure is seen.

due to the third harmonic of 267 nm (H3, $\sim$14 eV) acting as the pump.

The pump photon energy was also experimentally tuned by varying the phase-matching angle of the two β-BBO crystals from about 4.63 to 4.67 eV with a FWHM of about 0.03 eV. This corresponds to third harmonic central photon energies varying from 13.9 to 14.0 eV. The strongest 4.1 THz quantum beat was observed at the high-energy side of the tuning range (14.0 eV), and there was no quantum beat recorded on the low-energy side of the tuning range (13.9 eV). This observation is consistent with the known spectroscopy of nitrogen [20,21,24]. The states that are believed to be involved lie at 13.98 and 14.00 eV. The pump bandwidth is approximately 0.1 eV, as can be extrapolated from our previous work using a high-resolution time of flight electron spectrometer [25].

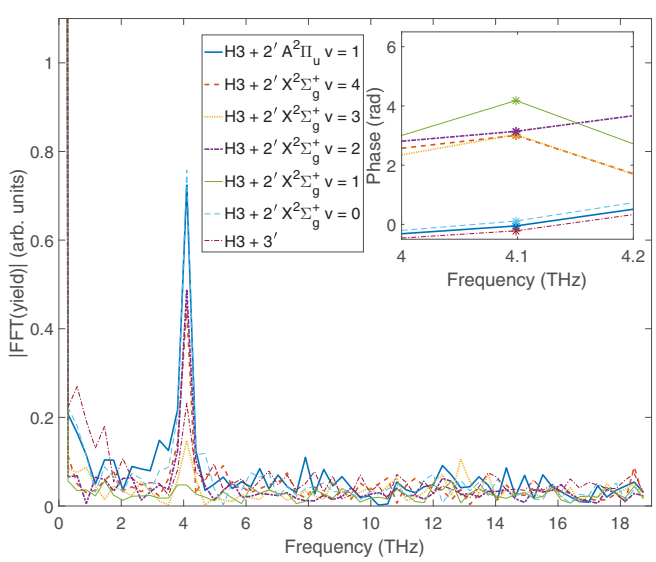

FIG. 5. Fourier amplitude of the photoelectron yield for $\tau >$ 0.6 ps. Each frequency bin is 0.29 THz wide. The relative phases of the different channels at 4.1 THz are seen in the inset, showing that there are two sets of oscillations that are approximately π out of phase with each other.

TRPES maps with the probe polarization perpendicular to the pump polarization were also done. The photoelectron yield oscillations were still present, and they were in phase with the parallel polarization cases.

The probe intensity was also varied from about 2×10^{12} W/cm^2 to 1×10^{13} W/cm^2 with 50 fs duration probe pulses. The 4.1 THz quantum beat was still observed at 2×10^{12} W/cm^2, which is only slightly higher than the intensity of the 400 nm probe, 1×10^{12} W/cm^2. This rules out any intensity-dependent effects of the 800 nm probe.

IV. PHOTOPHYSICS

We present here a straightforward phenomenological explanation of the time-resolved photoelectron spectrum observed with the 800 nm probe. Selected potential energy curves of N_2 are plotted in Fig. 7 and help illustrate the mechanism. The pump pulse, centered around 14 eV, prepares a superposition of the states $b'^1\Sigma_u^+$ $v = 13$ and $c_4'^1\Sigma_u^+$ $v = 4$ in N_2. The probe pulse comes at a later time τ and photoionizes the excited molecules with two probe photons at 800 nm. In the photoelectron spectrum, the electron kinetic energy is a direct indication of the final state of the corresponding cation. The final cationic states $X^2\Sigma_g^+$ $v = 0, 1, 2, 3, 4$ and $A^2\Pi_u$ $v = 0, 1$ are clearly resolved and are labeled [26] in Fig. 2(b) for the photoionization process involving a single third harmonic photon and two 800 nm probe photons (H3 + 2′). (Here we use the notation H3 to represent the third harmonic of the 267 nm driving pulse, i.e., the ninth harmonic of 800 nm; 2′ represents two 800 nm photons in the probe step.) The process involving the absorption of one third harmonic pump photon and three 800 nm probe photons (H3 + 3′) leads to observable but vibrationally unresolved features in Fig. 2. The H3 + 1′ process ends up energetically close to the continuum limit. We

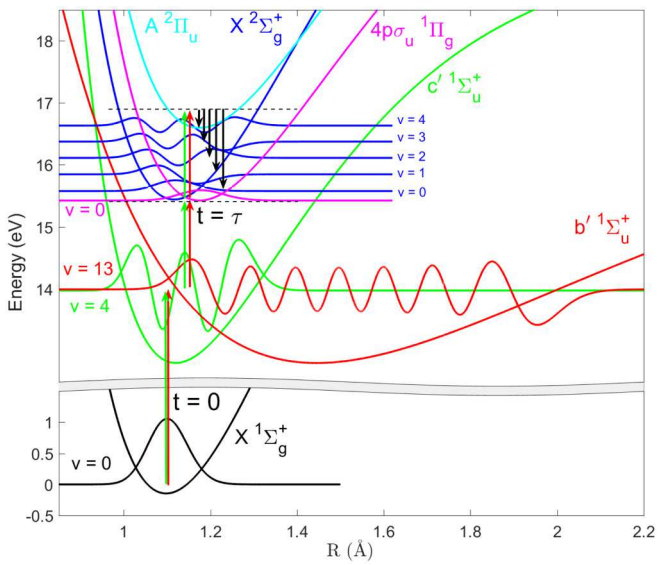

FIG. 7. Potential energy curves of various states of N_2 and N_2^+. Deperturbed diabatic excited state potentials [19] for $b'^1\Sigma_u^+$ and $c_4'^1\Sigma_u^+$ cross at $R = 1.2237$ Å and $E = 13.297$ eV. The two-pathway interference is represented by the green (light gray) and red (dark gray) arrows for H3 + 2′ ionization processes. The transitions at $t = 0$ are due to the pump pulse (13.98–14.00 eV) and the two-photon transitions at $t = \tau$ are due to the probe pulse with photon energy of 1.55 eV.

presumably observe only photoelectrons correlated to the final vibronic cationic ground state $X^2\Sigma_g^+ v = 0$ from this channel. In Fig. 5 the main observable feature, a peak at 4.1 THz, is seen in all selected channels with the exception of the $X^2\Sigma_g^+ v = 1$ where the signal is within the noise. Interestingly, the relative phases taken at 4.1 THz of the various channels bunch into two distinct groups with approximately π rad separation (Fig. 5 inset). One group of photoelectron is composed of the $X^2\Sigma_g^+ v = 0$ from the H3+n' ($n' = 2, 3$) ionization processes and of the $A^2\Pi_u^+ v = 1$ final state from the H3 + 2′ process. The second group corresponds to the final cationic states $X^2\Sigma_g^+ v = 2, 3, 4$ from the H3 + 2′ process.

The frequency of the observed quantum beat corresponds to the energy difference between the states $b'^1\Sigma_u^+ v = 13$ and $c_4'^1\Sigma_u^+ v = 4$. It can be explained in two equivalent qualitative ways. On the one hand, it is a realization of the two pathway interference so common to quantum mechanics. Starting from the same ground state $X^1\Sigma_g^+ v = 0$ and ending in the same final continuum state, pathways through $b'^1\Sigma_u^+ v = 13$ and $c_4'^1\Sigma_u^+ v = 4$ will accumulate different phases. Interference would appear in the photoelectron yield and angular distributions. This first picture does not quite explain the existence of two distinct groups with out-of-phase oscillations in the photoelectron yield.

The second way to look at it is more insightful into the physics of Rydberg and valence perturbations. The electronic states $b'^1\Sigma_u^+$ and $c_4'^1\Sigma_u^+$ have the same symmetry and perturb each other through the electrostatic interaction [18–21,27]. The first-order basis can be constructed from a subset of zeroth-order states as will be done in the next section. The perturbed (first-order) states (ψ_1 and ψ_2) each contain a large percentage of mixed character $b'^1\Sigma_u^+ v = 13$ and $c_4'^1\Sigma_u^+ v = 4$. The superposition created by the pump in the energy eigenstates (first-order) can then be projected onto the (nonorthogonal) zeroth-order basis. Zeroth-order populations oscillate back and forth at the frequency difference (4 THz). Assuming simple vertical transitions, Franck-Condon factors determine the ionization dynamics. Cationic channels with corresponding oscillations in the photoelectron spectrum then come in two groups: those oscillating in phase with the zeroth-order $b'^1\Sigma_u^+ v = 13$ state and those oscillating in phase with the zeroth-order $c_4'^1\Sigma_u^+ v = 4$ state.

TABLE I. Spectroscopic constants of nitrogen[a].

State	T_0 (cm^{-1})	R_e (Å)	ω_e (cm^{-1})	$\omega_e x_e$ (cm^{-1})	Ref.
$B^2\Sigma_u^+$	151 114.5	1.074	2419.84	23.18	[30]
$A^2\Pi_u$	134 820	1.1749	1903.7	15.02	[30]
$X^2\Sigma_g^+$	125 653.1	1.11642	2207	16.1	[30]
$b'^1\Sigma_u^+$	103 669.7	1.445	762.9	3.95	[31]
$c_4'^1\Sigma_u^+$	104 384.1	1.12	2193.1	22.07	[31]
$X^1\Sigma_g^+$	0	1.09768	2358.57	14.324	[30]

[a]T_0: minimum electronic energy; R_e: equilibrium internuclear distance; ω_e first term of vibrational constant; $\omega_e x_e$: second term of vibrational constant.

The photoelectron signals seen in Fig. 2(a) and Fig. 4 maintain the same amplitude up to at least a delay time of 10 ps (not shown). However, the modulation depth of the quantum beats decreases with time, with an exponential time constant of 2.5–4 ps as mentioned above (see Fig. 6). The loss of modulation depth is most likely due to rotational effects. The single-photon, dipole-allowed excitation process will select a subset of molecular alignments within the laboratory frame, producing rotational coherences in each electronic state. However, the two electronic states have significantly different rotational constants, as seen by the values of R_e listed in Table I. Therefore, the net excited state alignment will dephase on rotational timescales, reducing the modulation depth, as seen in the data.

The lack of a quantum beat with the 400 nm probe (Fig. 3) suggests that the 800 nm probe goes through a resonant state that acts as a Franck-Condon filter, rendering the quantum beat visible. Such intermediate resonance phenomena are commonly seen in the comparison of single-photon versus resonantly enhanced two-photon ionization of the same excited state wave packet, as was detailed previously for the case of SO_2 [28]. A candidate for this intermediate resonant state is suggested in the Discussion section.

V. THEORETICAL MODEL

A. Zeroth-order Hamiltonian

Throughout this analysis we work in the diabatic Born-Oppenheimer (BO) basis. The molecular Hamiltonian is defined as

$$\begin{aligned}\mathcal{H} &= T^N(R,\theta,\phi) + \mathcal{H}_{el} \\ &= [T^N(R) + \mathcal{H}^{\mathrm{ROT}}] + [T^e(r) + V(r,R)], \end{aligned} \tag{1}$$

$$V(r,R) = V^{eN}(r,R) + V^{ee}(r) + V^{NN}(R), \tag{2}$$

$$V^{ee}(r) = \sum_{\substack{i=1\\ j>i}}^{n} \frac{e^2}{r_{ij}}. \tag{3}$$

Here $\mathcal{H}_{el}$ is the electronic Hamiltonian, $T^N(R)$ is the nuclear kinetic energy operator, $\mathcal{H}^{\mathrm{ROT}}$ is the rotational energy Hamiltonian, T^e is the electron kinetic energy operator, and V is the electrostatic potential energy including electron-nucleus (V^{eN}), electron-electron (V^{ee}), and nucleus-nucleus (V^{NN}) interactions. The Coulomb potential corresponding to electron-electron repulsion is explicitly given in Eq. (3). In the diabatic basis, where electronic and vibration-rotation wave functions Φ_i^d and χ_v are separable,

$$\Psi_i^{BO} = \Phi_i^d(r,R)\chi_v(R,\theta,\phi). \tag{4}$$

The clamped nuclei electronic Schrödinger equation and the nuclear Schrödinger equations are, respectively,

$$[T^e(r) + V(r,R)]\Phi_i^d(r,R) = E_i^{el}(R)\Phi_i^d(r,R), \tag{5}$$

$$[T^N(R,\theta,\phi) + E_i^{el}(R)]\chi_v(R,\theta,\phi) = E_{v_i}\chi_{v_i}(R,\theta,\phi). \tag{6}$$

Here $E_i^{el}(R)$ is the diabatic potential energy curve associated with each electronic wave function Φ_i^d, and E_{v_i} the rovibronic energy associated with each vibrational wave function $\chi_{v_i}(R,\theta,\phi)$.

B. Potential energy curves

The proposed two-pathway interference to explain the observations is detailed in Fig. 7. The vibrational wave functions are also plotted on the same graph. The diabatic potential energy curves were modeled by Morse potentials [29] (Table I). The photoelectron yield and angular distribution oscillations were attributed to a set of two pathway electronic quantum interferences where the initial state is the ground vibronic state of the molecule $X^1\Sigma_g^+$ $v=0$, the two intermediate states are the highly vibrationally excited valence state $b'^1\Sigma_u^+$ $v=13$ and the Rydberg state $c_4'^1\Sigma_u^+$ $v=4$, and the final state is the ground state $X^2\Sigma_g^+$ $v=0,1,2,3,4$ or the first excited state $A^2\Pi_u$ $v=0,1$ of the cation.

Franck-Condon factors (FCFs), defined by

$$FCF_{ij} = |\langle\chi_{v_i}(R)|\chi_{v_j}(R)\rangle|^2, \tag{7}$$

express the part of the transition probability based on the vibrational part of the wave functions. They are given in Fig. 8(a) for the transitions from the ground state to the two intermediate states of interests for various vibrational levels. We note a two orders of magnitude difference between the probability for the $X^1\Sigma_g^+$ $v=0 \rightarrow b'^1\Sigma_u^+$ $v=13$ and the $X^1\Sigma_g^+$ $v=0 \rightarrow c_4'^1\Sigma_u^+$ $v=4$ transitions based on these (unperturbed) zeroth-order diabatic potential energy curves. These factors disagree with the high-resolution absorption spectrum of N_2, where both transitions have about equal probability [24]. These two intermediate states have the same electronic symmetry and perturb each other through a homogenous electrostatic interaction [18–21,27]. FCFs for transitions from the intermediate states to the ground cationic vibronic manifold and to the first electronically excited cationic manifold are also given in Figs. 8(b) and 8(c), respectively.

C. Perturbation

The BO approximation fails to describe the two strongly coupled electronic states $b'^1\Sigma_u^+$ and $c_4'^1\Sigma_u^+$. In the diabatic basis, interactions between states are induced by the electronic part of the Hamiltonian, $\mathcal{H}_{el}$. The Hamiltonian matrix is then

$$H_{ij} = \delta_{ij}\left(E_{v_i}^{el} + E_{v_j}^{i}\right) + V_{ij}. \tag{8}$$

If we assume a linear dependence of the matrix element H_{ij} on R, nuclear and electronic coordinates can be separated [32]. The off-diagonal elements can be written as

$$\begin{aligned} V_{ij} &= \left\langle\Phi_1^d\middle|\mathcal{H}_{el}\middle|\Phi_2^d\right\rangle_r\langle\chi_{v_i}(R)|\chi_{v_j}(R)\rangle \\ &= H_e\langle\chi_{v_i}(R)|\chi_{v_j}(R)\rangle. \end{aligned} \tag{9}$$

The deperturbation calculations are taken from Ref. [19]. A complete discussion about the nature of the electrostatic interaction between a valence and a Rydberg state which share the same symmetry but differ by two electron configuration orbitals can be found at Ref. [32]. The main perturbing term is the electron-electron repulsion [Eq. (3)]. To first order in perturbation theory, the exact energy eigenstates are obtained from the zeroth-order diabatic Born-Oppenheimer basis by adding off-diagonal coupling [Eq. (9)] corresponding to the electrostatic interaction. The coupling strength H_e was found to be 890 cm^{-1} [19], and $\langle\chi_{v_{b'}}(R)|\chi_{v_{c_4'}}(R)\rangle$ are vibrational wave-function overlap integrals between unperturbed $b'^1\Sigma_u^+(v_1)$ and $c_4'^1\Sigma_u^+(v_2)$ states. Diagonalization of this Hamiltonian yields both the total energy, which agrees with high-resolution spectroscopy measurements [19], and the eigenstates, which are linear superpositions of zeroth-order unperturbed vibronic states:

$$|\psi_i\rangle = \sum_{v_{b'}} c_{v_{b'}}^i\left|\Phi_{b'}^d\chi_{v_{b'}}\right\rangle + \sum_{v_{c_4'}} c_{v_{c_4'}}^i\left|\Phi_{c_4'}^d\chi_{v_{c_4'}}\right\rangle. \tag{10}$$

Expansion coefficients of the two vibronic states of interests, ψ_1 and ψ_2, in the zeroth-order diabatic basis are shown in Fig. 9. Twenty vibronic states are considered in the basis set, namely, $b'^1\Sigma_u^+$ $v=0$–14 and $c_4'^1\Sigma_u^+$ $v=0$–4. Factors analogous to FCFs can also be calculated for eigenstates formed from linear combinations of electronic states (Fig. 8, open circles), but then knowledge of the relative electronic dipole moment ratio between the states is required. In Fig. 8(a) (open circles), transitions from the N_2 ground state to the two first-order electronic states of interest were considered allowed and equally probable.

D. Projections to the final states

Description of the time-domain simulation follows. First, at time zero, the 14 eV pump pulse whose bandwidth covers both states impulsively populates the eigenstates $|b'^1\Sigma_u^+(13)\rangle$ and $|c_4'^1\Sigma_u^+(4)\rangle$ with equal probability and relative phase zero (set arbitrarily). This is a reasonable assumption from the pump pulse spectral bandwidth and the high-resolution

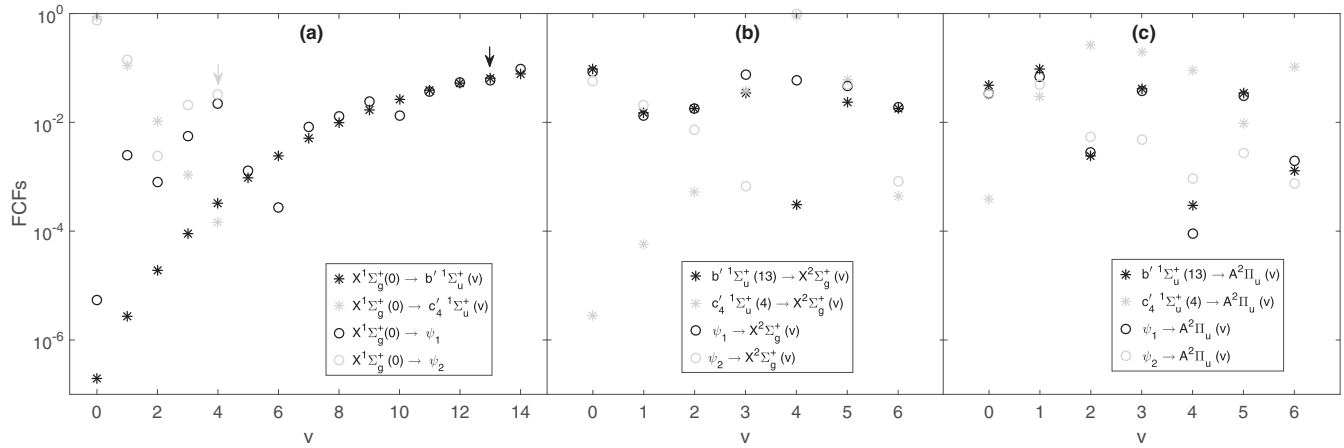

FIG. 8. Franck-Condon factors (FCFs) calculated between (a) the ground state of N_2 and the various vibrational states of either $b'^1\Sigma_u^+$ (black) or $c_4'^1\Sigma_u^+$ (gray). (b) FCFs calculated between the excited states of interest and the ground cationic state $X^2\Sigma_g^+$. (c) FCFs calculated between the excited states of interest and the first cationic excited state $A^2\Pi_u$. In all cases, zeroth-order diabatic (unperturbed, asterisk) and perturbed states (open circles) are considered.

absorption spectrum of nitrogen [24], which shows these lines have about equal absorption. It is also consistent with our FCFs calculations for the exact eigenstates to first order in perturbation theory [Fig. 8(a), open circles]. Since the probe step projects the wave packet onto the low-lying ionic states, which are well-behaved BO states, it is fruitful to expand the wave packet in the BO basis:

$$|\Psi(t)\rangle = \frac{1}{\sqrt{2}}|\psi_1\rangle e^{-iE_1t/\hbar} + \frac{1}{\sqrt{2}}|\psi_2\rangle e^{-iE_2t/\hbar}$$
$$= \sum_{v_{b'}} a_{v_{b'}}(t)\left|\Phi^d_{b'}\chi_{v_{b'}}\right\rangle + \sum_{v_{c_4'}} a_{v_{c_4'}}(t)\left|\Phi^d_{c_4'\Sigma_u^+}\chi_{v_{c_4'}}\right\rangle, \quad (11)$$

where $a_{v_{b'}}(t)$ and $a_{v_{c_4'}}(t)$ are the time-dependent coefficients for vibrational states v_1 and v_2 in the b' and c_4' diabatic states, respectively:

$$a_{v_n}(t) = \frac{1}{\sqrt{2}}\left(c^1_{v_n}e^{-iE_1t/\hbar} + c^2_{v_n}e^{-iE_2t/\hbar}\right). \quad (12)$$

Here $c^i_{v_n}$ are eigenstate expansion coefficients for the v_n diabatic state as in Eq. (10), and E_i are eigenstate energies. The diabatic state populations $|a_{v_n}|^2$ evidently oscillate at the frequency difference between the two perturbed eigenstates:

$$|a_{v_n}|^2(t) = \frac{1}{2}\left(\left|c^1_{v_n}\right|^2 + \left|c^2_{v_n}\right|^2 + 2c^1_{v_n}c^2_{v_n}\cos\Omega t\right),$$
$$\Omega = \frac{E_2 - E_1}{\hbar}. \quad (13)$$

All 20 basis state have some populations, but only the three most prominent are plotted in Fig. 10(a). The expected oscillatory behavior at the eigenstates frequency difference (3.96 THz) is observed. The probe pulse impulsively projects this wave packet at time τ onto the final states. For simplicity we consider only the one-photon ionization case here. In the weak field limit which assumes no population depletion and fixed intensity Dirac-shape probe pulse, the photoelectron yield from a single-photon probe process is proportional to [8]:

$$S_f(\tau) = |\langle\Psi_{\text{final}}|\boldsymbol{E}\cdot\hat{d}|\Psi(\tau)\rangle|^2. \quad (14)$$

In the diabatic basis for transitions to the $X^2\Sigma_g^+(v)$ continuum, this yields

$$S_{X(v)}(\tau) = \left|\boldsymbol{D}^X_{\boldsymbol{b'}}\sum_{v_{b'}} a_{v_{b'}}(\tau)\langle\chi_{X^2\Sigma_g^+(v)}|\chi_{b'}\rangle + \boldsymbol{D}^X_{\boldsymbol{c_4'}}\sum_{v_{c_4'}} a_{v_{c_4'}}(\tau)\left\langle\chi_{X^2\Sigma_g^+(v)}\middle|\chi_{v_{c_4'}}\right\rangle\right|^2, \quad (15)$$

where $\boldsymbol{D}^X_{\boldsymbol{n}} = \langle\boldsymbol{k},\epsilon;\Phi_{X^2\Sigma_g^+}|\boldsymbol{E}\cdot\hat{d}|\Phi^d_n\rangle$ are electronic dipole matrix elements between the neutral diabatic states n, and the ground ionic state. In the Franck-Condon (FC) approximation these are approximated as being independent of the nuclear coordinates, and therefore independent of ionic vibrational quantum number. Thus, if the FC approximation holds, these dipole matrix elements cannot effect the relative time-dependent behavior of the signal correlated to different ionic vibrational states. In order to investigate this behavior we can therefore set $\boldsymbol{D}^i_{\boldsymbol{b'}} = \boldsymbol{D}^i_{\boldsymbol{c_4'}} = 1$. The predicted photoelectron

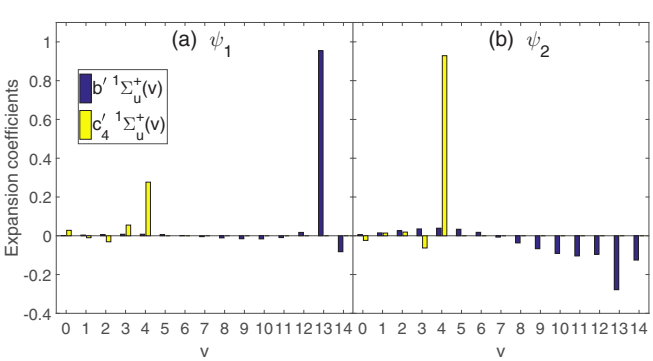

FIG. 9. Eigenstates (a) $|b'^1\Sigma_u^+(13)\rangle$ and (b) $|c_4'^1\Sigma_u^+(4)\rangle$ expansion in the zeroth-order diabatic basis.

TABLE II. Energy and electronic configuration of various states of the nitrogen and the nitrogen ion molecule.

ϵ (eV)	State	v	Configuration	Description
18.75[a]	$B^2\Sigma_u^+$	0	$(1\sigma_g)^2(1\sigma_u)^2(2\sigma_g)^2(2\sigma_u)^1(1\pi_u)^4(3\sigma_g)^2$	Second excited state of N_2^+
16.70[a]	$A^2\Pi_u$	0	$(1\sigma_g)^2(1\sigma_u)^2(2\sigma_g)^2(2\sigma_u)^2(1\pi_u)^3(3\sigma_g)^2$	First excited state of N_2^+
15.58[a]	$X^2\Sigma_g^+$	0	$(1\sigma_g)^2(1\sigma_u)^2(2\sigma_g)^2(2\sigma_u)^2(1\pi_u)^4(3\sigma_g)^1$	Ground state of N_2^+
15.54[a]	$4p\sigma_u\ ^1\Pi_g$	0	$(1\sigma_g)^2(1\sigma_u)^2(2\sigma_g)^2(2\sigma_u)^2(1\pi_u)^3(3\sigma_g)^2(4p\sigma_u)^1$	Rydberg state converging to $A^2\Pi_u$
			$(1\sigma_g)^2(1\sigma_u)^2(2\sigma_g)^2(2\sigma_u)^2(1\pi_u)^4(3\sigma_g)^1(3\sigma_u)^1$	High-lying valence state of N_2.
14.00[b]	$b'\ ^1\Sigma_u^+$	13		
			$(1\sigma_g)^2(1\sigma_u)^2(2\sigma_g)^2(2\sigma_u)^2(1\pi_u)^3(3\sigma_g)^2(1\pi_g)^1$	Configurations equally weighted
13.98[b,c]	$c_4'\ ^1\Sigma_u^+$	4	$(1\sigma_g)^2(1\sigma_u)^2(2\sigma_g)^2(2\sigma_u)^2(1\pi_u)^4(3\sigma_g)^1(4p\sigma_u)^1$	Rydberg state converging to $X^2\Sigma_g^+$
0[a]	$X^1\Sigma_g^+$	0	$(1\sigma_g)^2(1\sigma_u)^2(2\sigma_g)^2(2\sigma_u)^2(1\pi_u)^4(3\sigma_g)^2$	Ground state of N_2

[a]Reference [33].
[b]Reference [16].
[c]Reference [31] reports 80% $4p\sigma_u$, 10% $3p\sigma_u$, and 10% $3s\sigma_u$ content.

yields are plotted in Figs. 10(b) and 10(c). The quantum beat and π phase jumps between ionic vibrational are evident. The origin of these are discussed in the following section. In computing the $A\ ^2\Pi_u$ photoionization signals, we approximate transitions from zeroth order $b'\Sigma_u^+$ to $X^2\Sigma_g^+$ and $A\ ^2\Pi_u$ as being equally probable, i.e., $\boldsymbol{D}_{b'}^{X} = \boldsymbol{D}_{b'}^{A} = 1$, as they constitute a single configuration change from both electronic states. Transitions from zeroth order $c_4'\Sigma_u^+$ to $X^2\Sigma_g^+$ should be allowed as well (amplitude 1, phase 0), while transitions from $c_4'\Sigma_u^+$ to $A\ ^2\Pi_u$ are less likely (amplitude 0) due to the required

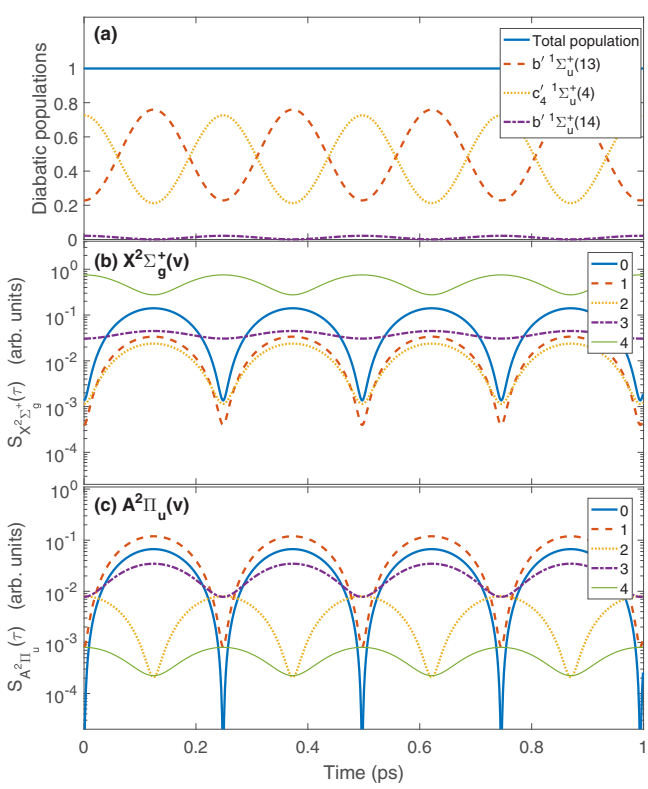

FIG. 10. Model predictions of vibrationally resolved excited state wave-packet projections onto (a) the excited state zeroth-order diabatic basis; (b) the ground cationic state; (c) the first cationic excited state.

two electronic configuration changes. The same assumptions were made to compute the eigenstates FCFs in Figs. 8(b) and 8(c). The electronic configuration of selected states is presented in Table II.

VI. DISCUSSION

The lack of a quantum beat when probing the wave packet at 400 nm (Fig. 3) is a striking feature in our data. Several possibilities could explain this lack of beat. First, the most plausible explanation is the presence of an additional resonant state in the 800 nm probe case at the $H3 + 1'$ level. For a homonuclear diatomic, electric dipole selection rules dictate a change of parity for a one-photon bound-bound transition. The ground state of N_2 has even parity ($X\ ^1\Sigma_g^+$). To be two-photon allowed by selection rules, this resonance just below the ionization potential has to have even ("g") symmetry. This state therefore cannot be observed in the linear absorption spectrum of N_2 because it is one-photon forbidden. Two families of Rydberg states possess the correct symmetry and energy to cause a resonance at the $H3 + 1'$ level when probed at 800 nm. Calculations have predicted a $4p\sigma_u\ ^1\Pi_g\ v = 0$ Rydberg state converging to the $A\ ^2\Pi_u\ v = 0$ at 15.54 eV, right in the bandwidth of the first probe photon [33]. One-photon excitation from the $c_4'^1\Sigma_u^+\ v = 4$ and the $b'^1\Sigma_u^+\ v = 13$ states to the state $4p\sigma_u\ ^1\Pi_g\ v = 0$ appears quite likely because they both require a single electronic molecular orbital configuration change (Table II). The calculated quantum defect of this state is 0.57, quite a large value, indicating that this state is not of pure Rydberg character [33]. A Rydberg series which also falls in the laser bandwidth is the $nd\pi_g\ ^1\Pi_g\ v = 0$ series converging to the $X\ ^2\Sigma_g^+\ v = 0$ state with n ranging from about 12 to infinity. Transitions to these states also require a single configuration change from both intermediate states. They should exhibit fairly good Rydberg character because of large principal quantum number. Ionization from these states should only lead to $X\ ^2\Sigma_g^+$ continuum.

The time-evolving Franck-Condon selectivity that gives rise to the observed quantum beats might occur in the transition moment governing the absorption of the first 800 nm photon. Second-photon photoionization from that intermediate manifold of separable high Rydberg states may then just occur vertically, ejecting electrons with velocities that track

the evolving first-photon overlaps as a function of pump-probe delay time. Sampling the same overall interval in a single (400 nm) photon transition projects the evolving 14 eV superposition onto the continuum, 1.5 eV above the adiabatic ionization threshold. Ion-core-continuum electron-configuration interaction there might somehow call for a flatter selection of core vibrational numbers as a function of time.

Second, energy degeneracy in the continuum would be lost, and hence no interference would be seen if the 400 nm probe laser bandwidth did not sufficiently cover the two excited states, separated by a mere 16 meV. Since this is not the case, this possibility can be ruled out. Third, if all probe processes are purely nonresonant, the lack of a quantum beat could be due to the different electronic dipole moments in the one-photon (400 nm) and two-photon (800 nm) probe processes. Particularly, our analysis of the data implies that ionization out of the diabatic states must be equally probable to nullify the oscillatory signal. This requires that the FC approximation fail for these transitions, since Fig. 8(b) indicates that the one-photon FCFs out of each state can be disparate.

We consider only the H3+2′ processes in the analysis that follows. Since the computations presented in Sec. V comprise numerous approximations, and represent only one-photon ionization, a direct comparison with the experiment cannot be made. However, the origin of the quantum beat in the signal and the π jumps in the phase of the oscillations as a function of ionic vibrational state can be understood. We consider the ionization signal correlated with each vibrational state of the $X\,^2\Sigma_g^+$ ionic state given by Eq. (15). This expands into population and coherence terms; those proportional to the population of vibrational states on the b' diabat, $|a_{v_{b'1}}(\tau)|^2$, those proportional to the population of vibrational states on the c_4' diabat, $|a_{v_{c_4'1}}(\tau)|^2$, and several inter- or intradiabat cross terms (coherences). Each population term is weighted by the ionization probability into the continuum: $|\boldsymbol{D}^{\boldsymbol{X}}_{\boldsymbol{b'}}\langle\chi_{X^2\Sigma_g^+(v)}|\chi_{v_{b'}}\rangle|^2$ for the b' diabat and $|\boldsymbol{D}^{\boldsymbol{X}}_{\boldsymbol{c_4'}}\langle\chi_{X^2\Sigma_g^+(v)}|\chi_{v_{c_4'1}}\rangle|^2$ for the c_4' diabat. Each weight determines the contribution of the population of a particular diabatic state to the signal, and therefore the amplitude and phase of the oscillation. Note that only the FCF part of each weight changes from one ionic vibrational state to the next, therefore the variation of amplitude and phase of oscillation across these states in the time resolved photoelectron spectrum must be attributable to the relative FCFs into each ionic state out of the b' and c_4' diabatic states. This is exemplified by our model.

Comparing Figs. 10(a) and 10(b) it is evident that the computed ionization signal is locked in phase with the oscillating population of either of the dominant diabatic states $c_4'^1\Sigma_u^+(4)$ and $b'^1\Sigma_u^+(13)$. The FCFs out of each of these states into the set of vibrational final states $X\,^2\Sigma_g^+(v)$ are shown in Fig. 8(b). Evidently ionization into $X\,^2\Sigma_g^+(0)$ is dominated by $b'^1\Sigma_u^+(13)$, which locks the phase of the oscillatory signal in this channel with the population of the $b'^1\Sigma_u^+(13)$ diabatic state. Higher up in the ionic vibrational manifold, the FCF out of $c_4'^1\Sigma_u^+(4)$ increases, adding a π-out-of-phase oscillatory contribution to the ionization signal, therefore reducing the amplitude. For $X\,^2\Sigma_g^+(3)$, the FCFs for each diabatic state are nearly equal, leading to a near-cancellation of the oscillatory component in the ion signal, which is evidently almost flat as a function of time [cf. Fig. 10(b)]. For ionization into $X\,^2\Sigma_g^+(4)$, the dominant contribution switches to $c_4'^1\Sigma_u^+(4)$ affecting a π jump in the phase of the oscillation from $X\,^2\Sigma_g^+(2)$ to $X\,^2\Sigma_g^+(4)$.

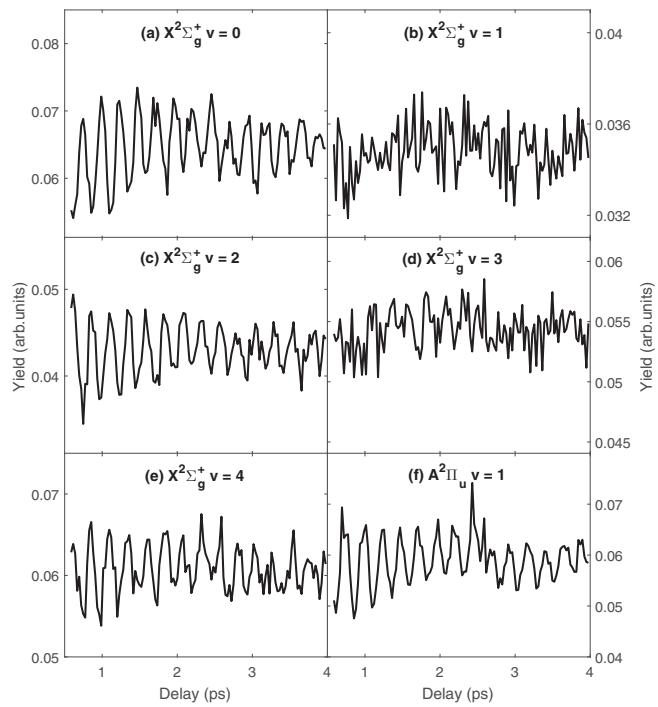

FIG. 11. Expanded view of the time-resolved photoelectron experimental spectrum corresponding to various final states plotted from 0.6 ps to 4 ps.

The above discussion focused on the populations of the diabatic states, neglecting the coherences between states. Since the wave packet predominantly consists of one vibrational state on each diabat, therefore we need worry only about the particular coherence between $b'^1\Sigma_u^+(13)$ and $c_4'^1\Sigma_u^+(4)$. This is proportional to the product of the amplitude coefficients of each state, $a_{4_{b'1}}(t)a^*_{13_{c_4'1}}(t)$, weighted by the product of the ionization dipoles and FCFs out of each state into the $X\,^2\Sigma_g^+(v)$ ionic state. The coherence term therefore makes a significant contribution only when the FCFs out of each state are comparable, adding an offset to the signal as well an oscillatory component. The offset can be seen for the $X\,^2\Sigma_g^+(3)$ ionization yields in Fig. 10(b), for which the oscillatory components cancel as discussed above. From this it is also evident that the oscillatory component of the cross term is relatively small. Therefore, the amplitude and phase of these signals are synchronized to the diabatic state populations.

We can apply the qualitative results of this model to the data plotted in Fig. 11. However, we must shift perspective somewhat, since two probe photons are required to ionize the excited state wave packet. This adds an additional step between the wave packet and the ionic vibrational states. Therefore the product of FCFs between the diabatic states and an unknown intermediate state and FCFs between the intermediate state and the ionic state modulate the ionization yield.

Nonetheless the same trends as those of the one-photon model can be spotted in the data. The signal corresponding to the $X\,^2\Sigma_g^+(0)$ state oscillates with the expected frequency and an initial phase of π. The $X\,^2\Sigma_g^+(1)$ state shows no appreciable oscillatory amplitude, and $X\,^2\Sigma_g^+(2)$ has a π phase change with respect to $X\,^2\Sigma_g^+(0)$. The initial 0 and π phases imply that the wave packet initiates in one of the diabatic states, which is expected since the absorption spectrum shows about equal absorption into the eigenstates, as assumed in the above model. The phase shift sequence is similar to the sequence exhibited by the computed signals $X\,^2\Sigma_g^+(2)$, $X\,^2\Sigma_g^+(3)$, and $X\,^2\Sigma_g^+(4)$ in the one-photon model. We can therefore deduce that $X\,^2\Sigma_g^+(0)$ and $X\,^2\Sigma_g^+(2)$ track the populations of different diabatic states, each having a favorable net FC overlap with the corresponding ionic state after including the possible intermediate states. Since the wave packet in the computation was initiated based on relative strengths of eigenstates in the absorption spectrum, it is likely the case that $X\,^2\Sigma_g^+(0)$ follows the b' diabatic population and $X\,^2\Sigma_g^+(2)$ follows the c_4' diabatic population. Further, $X\,^2\Sigma_g^+(1)$ which shows no oscillation must have equal two-photon FC overlap with each diabatic state, thus canceling the oscillatory component of the signal.

VII. CONCLUSION

In conclusion, we have observed the oscillation of the population at 4.1 THz between highly vibrationally excited valence and Rydberg states in the photoelectron spectrum of molecular nitrogen following deep ultraviolet excitation at 14.0 eV. A wave packet of molecular eigenstates was thus initially prepared that includes non-Born-Oppenheimer coupling. The field-free evolution of this quasi-two-level wave packet was observed through projections onto a multitude of vibrational cationic states. Photoelectrons corresponding to the $X\,^2\Sigma_g^+\ v=0, A^2\Pi_u\ v=0,1$ map the population of the zeroth-order $b'^1\Sigma_u^+\ v=13$ diabatic state, while $X\,^2\Sigma_g^+\ v=4$ maps the time-varying population of the diabatic $c_4'^1\Sigma_u^+\ v=4$ state. This work constitutes a clear example of the effect of long-lived non-Born-Oppenheimer effects on a relatively simple molecular system.

ACKNOWLEDGMENTS

We acknowledge the financial support from US Army Research Office Grant No. W911NF-14-1-0383. A.S. and D.M.V. thank the NSERC Discovery Grant program for financial support. We thank referee no. 2 for his or her valuable comments and suggestions.

[1] A. H. Zewail, J. Phys. Chem. A **104**, 5660 (2000).
[2] P. B. Corkum and F. Krausz, Nat. Phys. **3**, 381 (2007).
[3] L. Nugent-Glandorf, M. Scheer, D. A. Samuels, A. M. Mulhisen, E. R. Grant, X. Yang, V. M. Bierbaum, and S. R. Leone, Phys. Rev. Lett. **87**, 193002 (2001).
[4] A. Fleischer, H. J. Wörner, L. Arissian, L. R. Liu, M. Meckel, A. Rippert, R. Dörner, D. M. Villeneuve, P. B. Corkum, and A. Staudte, Phys. Rev. Lett. **107**, 113003 (2011).
[5] I. Fischer, D. M. Villeneuve, M. J. J. Vrakking, and A. Stolow, J. Chem. Phys. **102**, 5566 (1995).
[6] E. R. Warrick, J. E. Baekhoj, W. Cao, A. P. Fidler, F. Jensen, L. B. Madsen, S. R. Leone, and D. M. Neumark, Chem. Phys. Lett. **683**, 408 (2017).
[7] P. M. Kraus, S. B. Zhang, A. Gijsbertsen, R. R. Lucchese, N. Rohringer, and H. J. Wörner, Phys. Rev. Lett. **111**, 243005 (2013).
[8] A. Stolow, Annu. Rev. Phys. Chem. **54**, 89 (2003).
[9] A. Stolow, A. E. Bragg, and D. M. Neumark, Chem. Rev. **104**, 1719 (2004).
[10] V. Blanchet, M. Z. Zgierski, T. Seideman, and A. Stolow, Nature (London) **401**, 52 (1999).
[11] T. Suzuki, Annu. Rev. Phys. Chem. **57**, 555 (2006).
[12] A. Stolow and J. G. Underwood, Time resolved photoelectron spectroscopy of nonadiabatic dynamics in polyatomic molecules, in *Advances in Chemical Physics* (Wiley-Blackwell, New York, 2008), pp. 497–584.
[13] V. Blanchet, M. Z. Zgierski, and A. Stolow, J. Chem. Phys. **114**, 1194 (2001).
[14] M. Schmitt, S. Lochbrunner, J. P. Shaffer, J. J. Larsen, M. Z. Zgierski, and A. Stolow, J. Chem. Phys. **114**, 1206 (2001).
[15] S. T. Pratt, P. M. Dehmer, and J. L. Dehmer, J. Chem. Phys. **80**, 1706 (1984).
[16] S. T. Pratt, P. M. Dehmer, and J. L. Dehmer, J. Chem. Phys. **81**, 3444 (1984).
[17] G. S. Ondrey, C. Rose, D. Proch, and K. L. Kompa, J. Chem. Phys. **95**, 7823 (1991).
[18] J. M. Ajello, G. K. James, B. O. Franklin, and D. E. Shemansky, Phys. Rev. A **40**, 3524 (1989).
[19] H. Lefebvre-Brion, Can. J. Phys. **47**, 541 (1969).
[20] K. Dressler, Can. J. Phys. **47**, 547 (1969).
[21] D. Stahel, M. Leoni, and K. Dressler, J. Chem. Phys. **79**, 2541 (1983).
[22] C. Marceau, V. Makhija, D. Platzer, A. Y. Naumov, P. B. Corkum, A. Stolow, D. M. Villeneuve, and P. Hockett, Phys. Rev. Lett. **119**, 083401 (2017).
[23] G. A. Garcia, L. Nahon, and I. Powis, Rev. Sci. Instrum. **75**, 4989 (2004).
[24] P. Gürtler, V. Saile, and E. Koch, Chem. Phys. Lett. **48**, 245 (1977).
[25] C. Marceau, T. J. Hammond, A. Y. Naumov, P. B. Corkum, and D. M. Villeneuve, J. Phys. Commun. **1**, 015009 (2017).
[26] A. J. Yencha, K. Ellis, and G. C. King, J. Electron Spectrosc. Relat. Phenom. **195**, 160 (2014).
[27] P. K. Carroll and C. P. Collins, Can. J. Phys. **47**, 563 (1969).
[28] I. Wilkinson, A. E. Boguslavskiy, J. Mikosch, J. B. Bertrand, H. J. Wörner, D. M. Villeneuve, M. Spanner, S. Patchkovskii, and A. Stolow, J. Chem. Phys. **140**, 204301 (2014).
[29] P. M. Morse, Phys. Rev. **34**, 57 (1929).
[30] K. P. Huber and G. H. Herzberg, Constants of diatomic molecules (data prepared by Jean W. Gallagher and Russell

D. Johnson, III) in *NIST Chemistry WebBook*, NIST Standard Reference Database No. 69, edited by P. J. Linstrom and W. G. Mallard (National Institute of Standards and Technology, Gaithersburg MD, 2019).

[31] H. Lefebvre-Brion and C. M. Moser, J. Chem. Phys. **43**, 1394 (1965).

[32] H. Lefebvre-Brion and R. W. Field, in *Perturbations in the Spectra of Diatomic Molecules*, edited by H. Lefebvre-Brion and R. W. Field (Academic Press, Orlando, Florida, US, 1986), Chap. 4, pp. 176–242.

[33] P. Cremaschi, A. Chattopadhyay, P. Madhavan, and J. Whitten, Chem. Phys. **109**, 117 (1986).